Available online at www.sciencedirect.com
SCIENCE DIRECT®
Icarus 170 (2004) 113–124
ICARUS
www.elsevier.com/locate/icarus

Titan's surface and rotation: new results from Voyager 1 images

James Richardson,* Ralph D. Lorenz, and Alfred McEwen

Lunar and Planetary Laboratory, University of Arizona, 1629 E. University Blvd., Tucson, AZ 85721-0092, USA

Received 29 October 2002; revised 22 March 2004

Available online 12 May 2004

Abstract

We present an analysis of images of Saturn's moon Titan, obtained by the Voyager 1 spacecraft on November 8–12, 1980. Orange filter (590–640 nm) images were photometrically corrected and a longitudinal average removed from them, leaving residual images with up to 5% contrast, and dominated by surface reflectivity. The resultant map shows the same regions observed at 673 nm by the Hubble Space Telescope (HST). Many of the same albedo features are present in both datasets, despite the short wavelength (600 nm) of the Voyager 1 images. A very small apparent longitudinal offset over the 14 year observation interval places tight constraints on Titan's rotation, which appears essentially synchronous at 15.9458 ± 0.0016 days (orbital period $= 15.945421 \pm 0.000005$ days). The detectability of the surface at such short wavelengths puts constraints on the optical depth, which may be overestimated by some fractal models.

Keywords: Titan, surface, atmosphere; Satellites; Image processing

1. Introduction

1.1. Background

It is generally stated that the images from the Voyager 1 (VG1) close encounter with Titan in November of 1980, coming within a distance of 6490 km, failed to show the surface (Smith et al., 1981). Titan's vertically-distended atmosphere, laden with organic haze, appeared to completely obscure the surface at the relatively short wavelengths sensed by Voyager 1's Vidicon cameras; such that the only features observed were a north–south hemispheric albedo contrast, and a dark polar hood (Smith et al., 1981, 1982). In recent years, Titan's surface has been revealed by many different observers using near-infrared instruments. While these studies have generated surface maps with considerable contrast (around 30% at 2 microns), the spatial resolution (pixel scale) is ultimately limited by the great distance to Titan, and maps to date allow resolutions of only a few degrees ($\sim$ 150–300 km) per pixel or worse, corresponding to angular resolutions of 0.05 arcsec or so.

Motivated by the high pixel scale of the Voyager 1 images of Titan (10–42 km/pixel), the 'ground truth' albedo distribution established at longer wavelengths, and models that indicate a sensitivity to surface reflectivity even at visible wavelengths, selected Voyager 1 images have been re-examined to determine whether surface features can indeed be recovered from them. While the quality of the Voyager 1 data is limited (the images are of only modest signal-to-noise) and the optical properties of the atmosphere make the surface only marginally detectable, this study may help to understand the haze limitations on the resolution of detectable surface contrasts by Cassini's Imaging Science Subsystem (ISS). Additionally, the results may be useful for comparison with other ground-based or spaceborne imaging, such as in constraining Titan's rotation period. Finally, this study may be of some historical interest in overturning the accepted wisdom regarding the Voyager data. We also conjecture that the human eye (having a visible wavelength range similar to Voyager), with appropriate filtering, may also be capable of sensing surface contrasts on Titan.

1.2. Detectability of Titan's surface at red wavelengths

Some years after the Voyager encounters, it was realized that Titan's surface should be detectable in the near-infrared; an understanding borne out first by disk integrated light-curves showing a longitudinal brightness variation

* Corresponding author. Fax: (520)-621-2933.
E-mail address: jrich@lpl.arizona.edu (J. Richardson).

0019-1035/$ – see front matter
doi:10.1016/j.icarus.2004.03.010

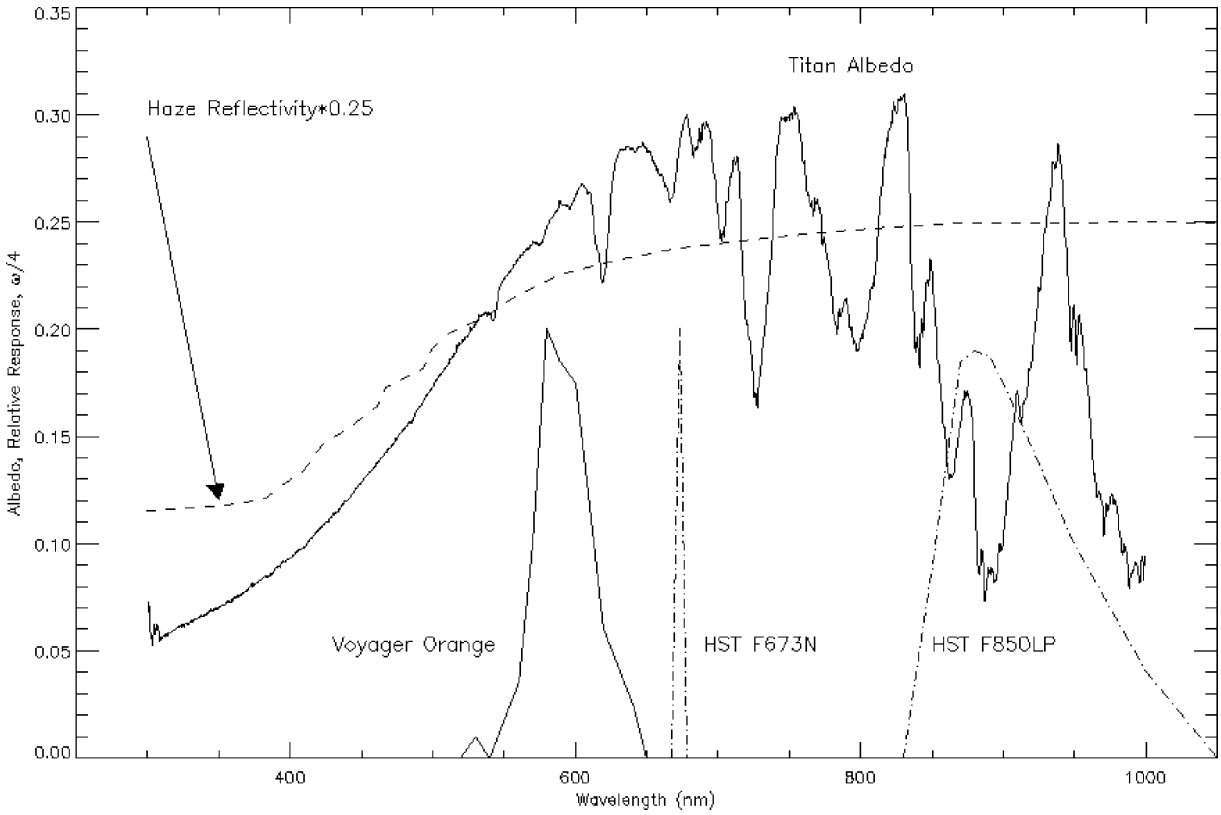

Fig. 1. Relative response of the Voyager 1 orange filters (NA and WA cameras) and the HST filters used to make the maps shown in this paper, compared with an albedo spectrum from Karkoschka (1995) for reference. Also shown is the single scattering albedo, ω, for tholin particles computed by McKay et al. (1989). Despite the relatively short wavelength, the single scattering albedo in the Voyager 1 orange filter range is still quite high (~ 0.88) and hence, most light is scattered rather than absorbed. It is likely that Titan's surface can be detected at all wavelengths longward of 600 nm except in methane absorption bands, not just in the prominent window at 940 nm.

(Lemmon, 1993; Lemmon et al., 1995; Noll and Knacke, 1993; Coustenis et al., 1995; Griffith, 1993) in 'windows' at 0.94, 1.07, 1.28, 1.58, and 2 microns, i.e., between the methane absorption bands. Subsequent high-resolution observations in these windows by the refurbished Hubble Space Telescope (HST) (Smith et al., 1996) yielded a map of Titan's relative surface reflectivity, most notably using the Wide-Field Planetary Camera 2 (WFPC2) with an 850 nm long pass filter, sampling the 0.94 micron window. The same gross albedo distribution is indicated in the other windows observed by (1) the HST/WFPC2 at 1.07 microns and (surprisingly) at 0.67 microns; (2) the HST Near Infrared Camera and Multi-Object Spectrometer (NICMOS) at 1.08, 1.65, and 2.04 microns (Meier et al., 2000); (3) ground-based speckle imaging with the Keck Telescope at 1.6 and 2.1 microns (Gibbard et al., 1999); (4) adaptive optics imaging with the Canada–France–Hawaii Telescope (CFHT) at 1.29 and 1.6 microns (Coustenis et al., 2001); and (5) adaptive optics imaging with the European Southern Observatory's (ESO) 3.6-m telescope at 2 microns (Combes et al., 1997). The contrast of surface features increases at progressively longer wavelengths because the optical depth of the haze becomes relatively low (around 2 at 1 micron, perhaps around 0.2 optical depths at 2 microns). However, as pointed out by Lorenz and Lunine (1997), radiative transfer models (McKay et al., 1989; Lemmon, 1994; Tomasko et al., 1989; Stammes, 1992) do show a sensitivity, albeit small, for observed albedo to surface reflectivity near 600 nm.

Two factors limit the visibility of the surface at these short wavelengths. First, the ratio of haze particle size to the wavelength becomes large, and hence the optical depth of the haze increases at short wavelengths. Of those photons reaching the surface, only $e^{-\tau}$ (where $\tau =$ vertical optical depth) will escape again without undergoing intermediate scattering events, severely degrading surface resolution through the combination of scattered and unscattered light. The implications of this study (using the Voyager 1 data) with regard to the optical depth will be discussed further in Section 3.4. The second, and here perhaps more crucial effect, is due to the optical properties of the material from which the haze is made: Titan owes its reddish color to the dramatic rise in single-scattering albedo of the haze particles from 400 to 600 nm, a rise in turn due to the remarkable drop in the imaginary part of the complex index of refraction of tholin material over this range (Khare et al., 1984). The challenge in imaging Titan's surface is not so much that the light reflected from the surface is undetectably weak, but that it is swamped by light scattered by the haze (that does not reach

Table 1
Selected Voyager 1 ISS orange filter images of Titan

Image No.	Camera	Date	Time (UT)	Texp (sec)	Phase (deg)	Res. (km/pixel)	Res. (pixel/deg)	N lat.	W long.	Final
3482402	Narrow	11/08/80	23:46:58	5.76	25.69	42.02	1.07	7.55	98.08	yes
3483415	Narrow	11/09/80	07:57:22	5.76	26.58	37.25	1.21	7.63	104.87	yes
3483914	Narrow	11/09/80	11:56:34	2.88	26.99	34.94	1.29	7.68	108.20	no
3484425	Narrow	11/09/80	16:05:22	5.76	27.42	34.56	1.38	7.73	111.87	yes
3485211	Narrow	11/09/80	22:18:10	2.88	28.04	29.02	1.56	7.81	116.90	no
3486216	Narrow	11/10/80	06:22:10	2.88	28.76	24.49	1.84	7.92	123.74	yes
3487016	Narrow	11/10/80	12:56:10	5.76	29.30	20.96	2.14	8.02	129.22	yes
3487526	Narrow	11/10/80	16:56:34	2.88	29.60	18.70	2.40	8.09	132.82	no
3488311	Narrow	11/10/80	23:06:10	2.88	30.07	15.40	2.91	8.19	138.16	no
3488315	Narrow	11/10/80	23:09:22	5.76	30.04	15.38	2.92	8.19	138.21	yes
3488537	Narrow	11/11/80	01:02:58	3.84	30.24	14.38	3.12	8.22	139.86	no
3491532	Wide	11/12/80	00:58:58	1.92	32.18	16.99	2.64	8.62	160.38	yes
3491648	Wide	11/12/80	01:59:46	1.92	32.57	13.35	3.37	8.65	160.96	yes
3491753	Wide	11/12/80	02:51:46	1.92	33.17	10.14	4.43	8.68	161.26	yes

the surface). Only by satisfactorily removing this component can the surface features be extracted. Implicit in this process is the assumption that the atmospheric component of the light has no significant variation over short horizontal length scales.

The partial map at 673 nm produced by Smith et al. (1996) does successfully show contrasts (features) that broadly match the distribution of reflectivity measured at longer, clearer wavelengths. The peak contrast observed was about 2%, although that map does not cover the darkest regions on Titan and the bright region on Titan's leading hemisphere was not centered in the disk. Hence contrasts due to surface effects at this wavelength should be somewhat larger than 2%.

The purpose of this study was to revisit the Voyager 1 1980 flyby images of Titan, and utilize the image processing techniques recently developed by Smith et al. (1996) and Meier et al. (2000) to extract surface features from images which are dominated by a strong atmospheric component. The resulting features were then validated by comparison with previous studies, and investigated for additional features and details (considering the much higher pixel scale at which Voyager 1 was able to image Titan as compared to ground-based or Earth-orbiting instruments). Finally, the rotation period of Titan was investigated, taking advantage of the 14 year time span between the Voyager 1 flyby of Titan in 1980 and the HST observations conducted in 1994 by Smith et al. (1996).

2. Image processing methodology

2.1. Image selection

The useful Voyager 1 images of Titan for this study were those taken with the Imaging Science Subsystem's (ISS) Vidicon-based Narrow Angle (NA) and Wide Angle (WA) cameras, equipped with an orange interference filter (Filter 3-ORANGE for the NA camera, and Filter 7-ORANGE for the WA camera (Instrument Catalogue NA1, 2000; Instrument Catalogue WA1, 2000). This arrangement yields a useful instrument response over the wavelength range of 590–640 nm, and peaking at roughly 600 nm (Danielson et al., 1981). Figure 1 shows the relative response of the Voyager 1 orange filters and the HST filters used to make the maps shown in this paper, compared with a reflection spectrum for Titan from Karkoschka (1995) for reference. Also shown is the single scattering albedo, ω, for tholin particles computed by McKay et al. (1989). Despite the relatively short wavelength, the single scattering albedo in the Voyager 1 orange filter range is still quite high (~ 0.88) and hence, most light is scattered rather than absorbed. It is likely that Titan's surface contributes to the reflectance at all wavelengths longward of 600 nm except in methane absorption bands, not just in the prominent window at 950 nm.

The Voyager 1 image set contains 91 orange filter images of Titan, for which the following selection criteria were used:

(1) Good spacecraft position, camera pointing, and calibration information must be available, via the ISIS (Integrated Software for Imagers and Spectrometers, available from USGS, Flagstaff) *naiflib* and *spicelib* procedures.
(2) The Titan disk must be at least ~ 120 pixels across in the image, (i.e., covering at least 15% of the field of view).
(3) The full Titan disk must be visible in the image (no partial images) to permit good limb fitting and co-registration of the calibrated images.

Of the 91 orange filter images taken by Voyager 1 (VG1 ORANGE), only 14 met all three of these criteria. The basic exposure information on these images is listed in Table 1. It may be possible at a later date to process some of the closest-approach, partial-disk Titan images (as well as images from Voyager 2), but for this investigation the emphasis was placed upon developing a convenient procedure for ex-

tracting the surface component from the low phase-angle, full-disk images and validating it with the previous results from other studies.

2.2. Processing technique

The six basic stages used to extract the 'surface component' from the 14 selected VG1 ORANGE images are demonstrated in Fig. 2, and are explained in the following paragraphs:

Figure 2, step (a) shows WA camera image no. 3491532 (see Table 1) following Level 0 (raw file conversion) and Level 1 (radiometric calibration, geometric correction, and Reseau mark removal) processing, performed using the ISIS package. At this stage, a manual limb-fit procedure was performed to improve the registration of the image.

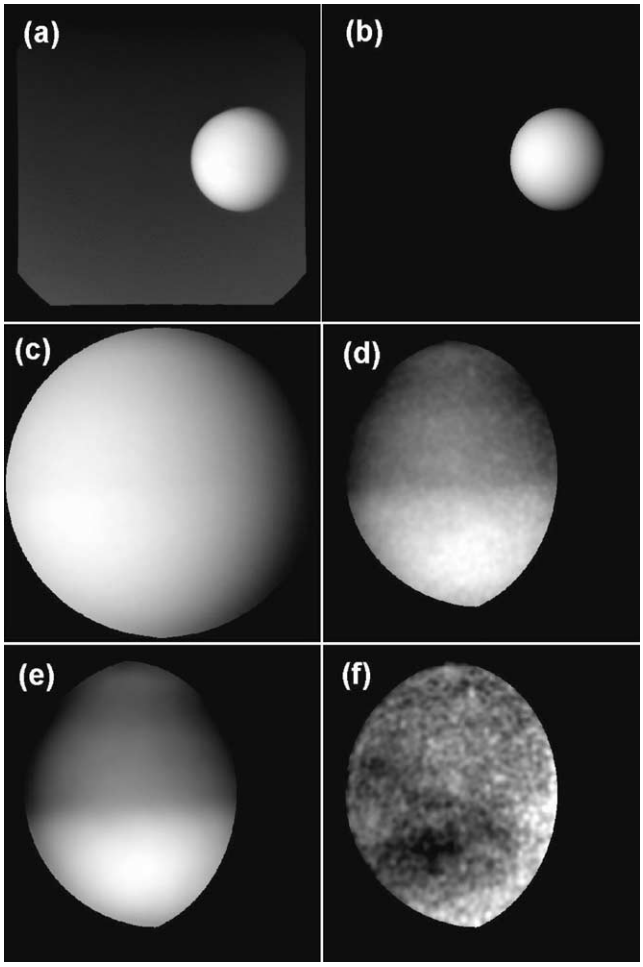

Fig. 2. An example of the six basic stages used to extract the 'surface component' from the 14 selected Voyager 1 orange filter images: (a) pre-processed image, calibrated and with Reseau marks removed, (b) synthetic image used to properly register the true image, (c) 'normalized' image, orthographically projected to an equatorial view at a center resolution of 5 pixel/degree, (d) photometrically corrected image, showing the north/south albedo dichotomy of the Titan atmosphere and a north polar hood, (e) the longitude-smeared average of all 14 images, used to represent the 'atmospheric component,' and (f) the final stretched and trimmed image, showing the division of the selected image (step (d)) by the 'atmospheric component' image (step (e)) and displaying about 5% maximum contrast. This image shows the 'spit' region and the two dark regions north and south of the equator west of 180° longitude (see Fig. 5).

Figure 2, step (b) shows a corresponding synthetically produced "Titan" image, modeling Titan as a Lambertian sphere placed at the position, range, and phase angle specified by the calibrated image header information from step (a). The calibrated image in step (a) was then co-registered with this synthetic image to further improve the calibrated image's position information.

Figure 2, step (c) shows the 'normalized' image, which has been orthographically re-projected to an equatorial view, centered at the subspacecraft Titan longitude, and having a center resolution of 5.0 pixel/degree (9 km/pixel). The background and near-limb portions of the image have also been removed. All 14 images in the series were placed in this same projection, at the same apparent resolution (5.0 pixel/degree or 9 km/pixel), and all having an equal 8-bit dynamic range (stretch). The resolution selected is just beyond the best resolution for the image series (which ranges from 10 to 42 km/pixel), such that the first images in the series are over-sampled (using bilinear interpolation) by a factor of about 5 (1.0 pixel/degree), and the last images in the series are over-sampled by a factor of about 1.1 (4.4 pixel/degree)—preserving the detail in the best images. As Table 1 shows, the phase angle of all of these images falls within a relatively narrow band (about 25°–33°), such that the terminator remains nearly stationary throughout the series of normalized images, despite the fact that the images range over a 63° band of subspacecraft longitudes (from 98°–161° W).

Figure 2, step (d) shows the photometrically corrected image, displaying the north/south albedo dichotomy of the Titan atmosphere and its north polar hood. Due to the nearly constant phase angle present throughout this image series (listed in Table 1), the photometric correction function utilized in this step was a simple lunar-Lambert function, discussed in McEwen (1991), which is given as:

$$I = I_o\left(2L\frac{\cos(\iota)}{\cos(\iota)+\cos(\varepsilon)} + (1-L)\cos(\iota)\right)^{-1}, \qquad (1)$$

where

I = final pixel value,

I_o = initial pixel value,

L = lunar-Lambert coefficient (0–1.0),

ι = light incidence angle,

ε = light emission angle.

The value of the lunar-Lambert coefficient, $L = 0.40$, was selected through trial-and-error (in 0.05 increments) to consistently minimize the effect of limb-darkening (to the left) and terminator brightening (to the right), to produce as 'flat' an image series as possible. The goal of this selection was to

find a single L value which minimized the pixel value standard deviation in a majority of the selected images (therefore applying a uniform photometric correction to all). At this stage, the images were also re-trimmed to sunlight incidence angles of $\iota < 80°$ and reflected light emission angles of $\varepsilon < 80°$.

Figure 2, step (e) shows the longitude-smeared, stacked average of all 14 images, which is used to represent the 'atmospheric component' of this image series. Averaging over the 63° of rotation present in the series effectively 'smears out' the longitudinal variation present in individual images, assumed to be primarily due to surface albedo variation, while preserving the latitudinal variation, assumed to be primarily due to atmospheric albedo variation. In the next step, this atmospheric component is then removed from each of the individual images in order to extract their effective 'surface component' (Smith et al., 1996). There are two forms of low-order variation in surface albedo which could inadvertently be included in the atmospheric component, and therefore removed in the final step. These are:

(1) surface latitudinal zoning (uniform over all longitudes), such as in the case of a polar cap, will be completely removed when the surface component is extracted using this method (Smith et al., 1996), and
(2) due to the limited rotation in this image series (63°) large-scale surface longitudinal zoning, such as in the case of a surface albedo feature covering many degrees of longitude, will artificially bias the brightness of the atmospheric component within affected latitudes and cause either under or over removal of the atmosphere when the surface component is extracted.

Since most low-order albedo zoning, especially in latitude, will more likely represent banding or zoning in the atmosphere rather than the surface, it is assumed that this removal process does not significantly affect the remaining (desired) surface component, although the limitations of this procedure must be borne in mind.

Atmosphere removal is performed using the image division technique (rather than image subtraction) because it adjusts for differences in overall intensity while extracting the information which is uncorrelated between the two images. Taking the ratio of the selected image (step (d)) to the 'atmospheric component' image (step (e)), produces a final 'surface component' image (step (f)). This particular image shows a portion of the dark regions to the west of the 'spit' (see Fig. 5). The final image series displays a rather low (but expected) dynamic range of about 2–5% contrast. At this stage, the image has been re-trimmed to sunlight incidence angles of $\iota < 60°$ and reflected light emission angles of $\varepsilon < 60°$. The image has also been re-stretched to improve its dynamic range and contrast.

Following processing, all of the images were examined for potential surface features. As expected at this low contrast level, the poor signal-to-noise ratio (especially with several of the NA camera images) was problematic, and led to the rejection of 5 of the 14 images (although vague surface features could be detected in *all* of the images). The final nine images, identified by a 'yes' annotation Table 1, were then stack averaged (first in groups of three, and then all nine) to further improve their signal-to-noise ratios and to enhance the 'real' features common to all images covering the same longitude range. This step produced three final regional views (centered at 120° W, 150° W, and 180° W longitude), and a complete map covering the longitude range of between roughly 75° W and 210° W, a latitude range of between roughly 45° N and 35° S, for a total coverage of about 24% of Titan's surface.

3. Discussion of results

3.1. Regional views

Figure 3 (left column) shows the three regional views produced by the process described in Section 2, displayed using a 'red-temperature' color gradient scale, as compared to map projections of the same regions produced by the HST F673N filter (center column) and HST F850LP filter (right column). The HST data sets are the same as those which were presented in Smith et al. (1996), but using different projections and color gradient scales for this presentation. Arrows on the VG1 ORANGE images track the rotation of two prominent portions of the Titan bright region (areas A2 and A3 in Fig. 5) along their high contrast border with a dark sickle shaped region (area B in Fig. 5). These regional views are discussed in detail below.

The left image in the upper row of Fig. 3 shows an average of the first three images in the final series of nine (taken with the NA camera), and is centered on the equator at 120° west (W) longitude (image information listed in Table 1). The most prominent feature in this regional view is the well-known Titan bright region, which appears brighter in these images than in any of the subsequent images. This feature is resolved into a roughly triangular shape, having a sharp, high contrast boundary (marked with arrows) on its western edge with a broad dark lane which comes into better view in the next regional view. The bright region displays a long eastward extension, such that it runs $\sim$ 2250 km along the equator from its boundary with the dark lane (near 130° W long.) to its eastern most point (near 80° W long.). The overall shape and position of the bright region in this regional view agrees well with the images obtained by the Hubble Space Telescope (Smith et al., 1996; Meier et al., 2000), the Keck Telescope (Gibbard et al., 1999), and the ESO 3.6-m telescope at La Silla (Combes et al., 1997).

The left image in the center row of Fig. 3 shows an average of the middle three images in the final series of nine (taken with the NA camera), and is centered on the equator at 150° west longitude. The most prominent feature in these images is what we have nicknamed the 'sickle,' a wide dark

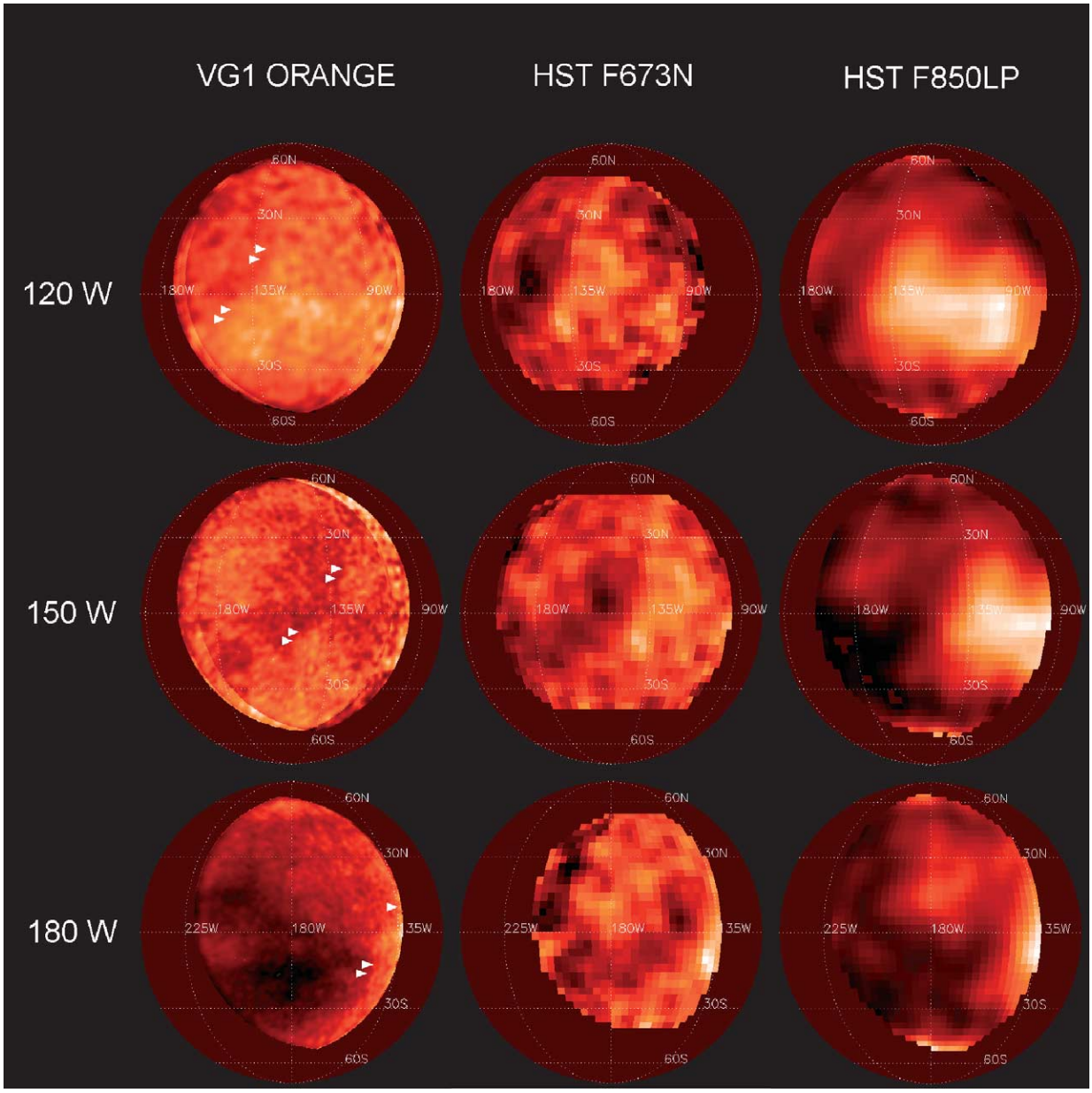

Fig. 3. (Left column) Three views of Titan's surface from the VG1 ORANGE filter (∼ 600 nm), displayed using a 'red-temperature' color gradient scale, as compared to similar map projections from (center column) the HST F673N filter (673 nm), and (right column) the HST F850LP filter (940 nm). From top to bottom, these regional views show: (top row) an average of the first three images in the series, centered on 120° W longitude and showing the Titan bright region at low sunlight incidence and emission angles, (center row) an average of the three middle images in the series, centered on 150° W longitude and showing the large 'sickle' shaped dark lane just to the west of the bright region, and (bottom row) an average of the three final images in the series, centered on 180° W longitude and showing the two very dark regions to the west of the Titan 'spit' region. Arrows on the VG1 ORANGE images track the rotation of two prominent portions of the Titan bright region (areas A2 and A3 in Fig. 5) along their high contrast border with the dark 'sickle' region. This figure can also be viewed at: http://www.lpl.arizona.edu/~jrich/Titan/regional.gif.

lane that runs diagonally southwest to northeast across the Titan surface, beginning near the very dark region labeled D2 in Fig. 5 and wrapping up and around the Titan 'spit' region described by Smith et al. (1996). The eastern edge of this lane forms a rather sharp boundary with the Titan bright region (marked with arrows), while its western edge is softer, having a less well defined boundary with the 'spit' region. The western edge of the Titan bright region is clearly visible in this image, although its brightness (moving to the east) is rather diminished in this regional view, most likely due to the very low incidence and emission angles, but perhaps also due to inaccurate atmospheric component extraction (see Section 2.2). Nonetheless, several of the small albedo features forming the boundary between the bright region and the 'sickle' are consistent from the previous view (top row) to this one—demonstrating that these are real features. The presence of such common features lends confidence to this extraction method and indicates that at least in areas of high

contrast, features of about 2°–3° in size (90–135 km) can be resolved through the haze in the VG1 images (although most identifiable features are larger).

The left image in the bottom row of Fig. 3 shows an average of the last three images in the final series of nine (taken with the WA camera), and is centered on the equator at 180° west longitude. These WA camera images were taken over a smaller subspacecraft longitude range than the previous sets, and thus show a smaller region of the surface. The most prominent features in this view are the two large *very* dark regions located north and south of the equator and to the west of the 'spit' region (labeled D1 and D2 in Fig. 5). These are the darkest features observed in the entire series, and display a complex shape and structure that is very consistent from individual image to image. These dark regions are also prominent in speckle observations at 2.1 and 1.6 microns (Gibbard et al., 1999). That work determined that the surface reflectivity of the dark material is less than 0.05, consistent with deposits of liquid hydrocarbons (i.e., 'ethane seas') or solid organics as on Iapetus. The general shape of these dark regions is also in good agreement with the Smith et al. (1996) results.

3.2. Map views

Figure 4 shows three cylindrically projected map views of the Titan surface features, consisting of (top) a stacked average of all nine of the final VG1 ORANGE filter images produced by this study using methane windows in the 590–640 nm range, (center) the HST F673N filter using methane windows near 673 nm (Smith et al., 1996), and (bottom) the HST F850LP filter using the methane window at 940 nm (Smith et al., 1996): all are displayed using a 'red temperature' color gradient scale. The maps all show good general agreement, especially the top two, which were made at similar wavelengths. The Titan 'bright region,' the 'sickle' shaped dark lane on its western flank, the smaller 'spit' region, and the two dark regions to the west of the 'spit' are visible in all three map views.

To further emphasize the most consistent features in the VG1 ORANGE map (top row, Fig. 4), Fig. 5 shows a map drawing produced from the VG1 ORANGE images of the Titan surface albedo features, and covering about 24% of the Titan surface. The identified features on this map are:

- (A1) the Titan bright region eastern extension,
- (A2) the Titan bright region northern area,
- (A3) the Titan bright region southwestern area,
- (B) the widest portion of the dark lane called the 'sickle,'
- (C) the center of the 'spit' region, with north, east, and west brighter areas,
- (D1) the northern very dark region, west of the 'spit,'
- (D2) the southern very dark region, west of the 'spit,' and south of area C.

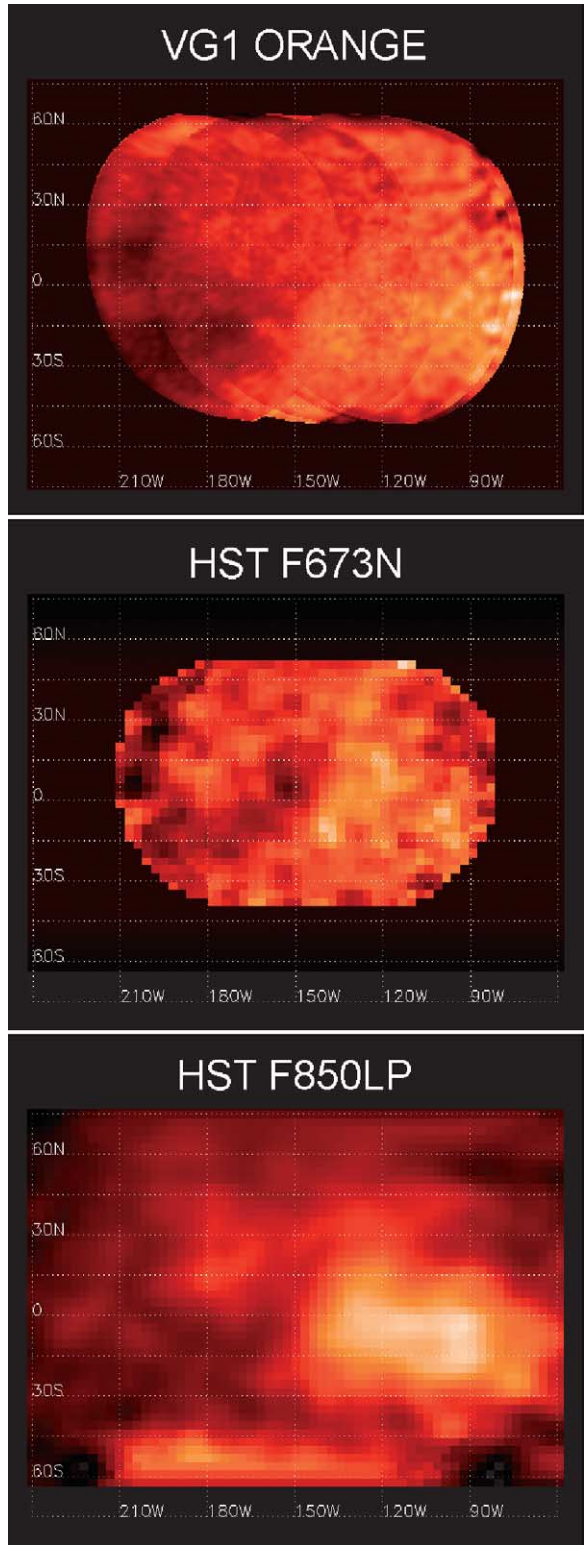

Fig. 4. Three cylindrically projected map views of the Titan surface features (displayed using a 'red-temperature' color gradient scale), as imaged by (top) the VG1 ORANGE filters at 590–640 nm, (center) the HST F673N filter at 673 nm (Smith et al., 1996), and (bottom) the HST F850LP filter using the methane window at 940 nm (Smith et al., 1996). These maps all show good general agreement, especially the top and center, which were imaged at similar wavelengths. This figure can also be viewed at: http://www.lpl.arizona.edu/~jrich/Titan/mapcombine.gif.

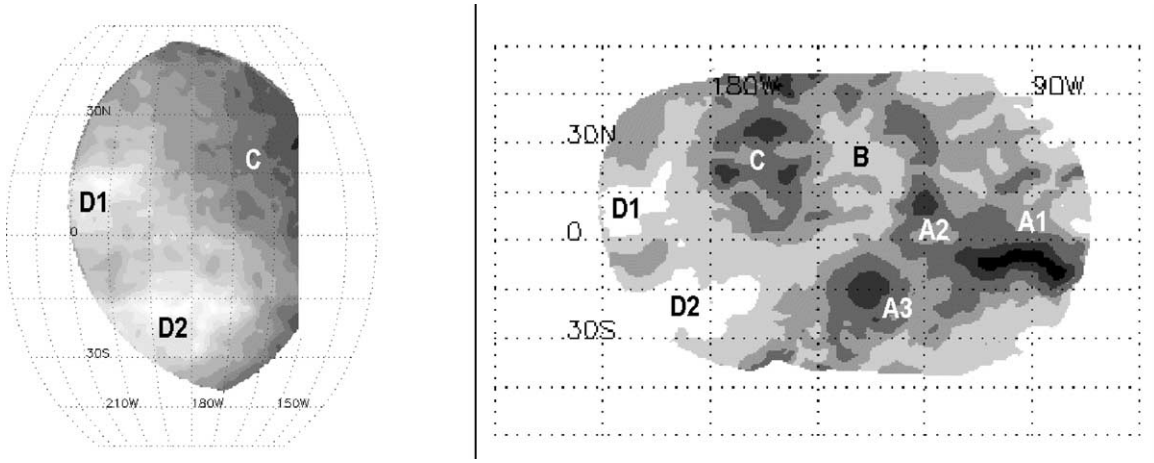

Fig. 5. Two map drawings produced from the VG1 ORANGE images of the Titan surface albedo features, covering about 24% of the Titan surface, and shown using a six-level, gray, negative gradient scale. Bright regions are shown with white labels while dark regions are shown with black labels. The identified features are: (A1) the Titan bright region eastern extension, (A2) the Titan bright region north point, (A3) the Titan bright region southwestern area, (B) the widest portion of the dark lane called the 'sickle,' (C) the center of the 'spit' region, with north, east, and west brighter areas, (D1) the northern very dark region, west of the 'spit,' and (D2) the southern very dark region, west of the 'spit.'

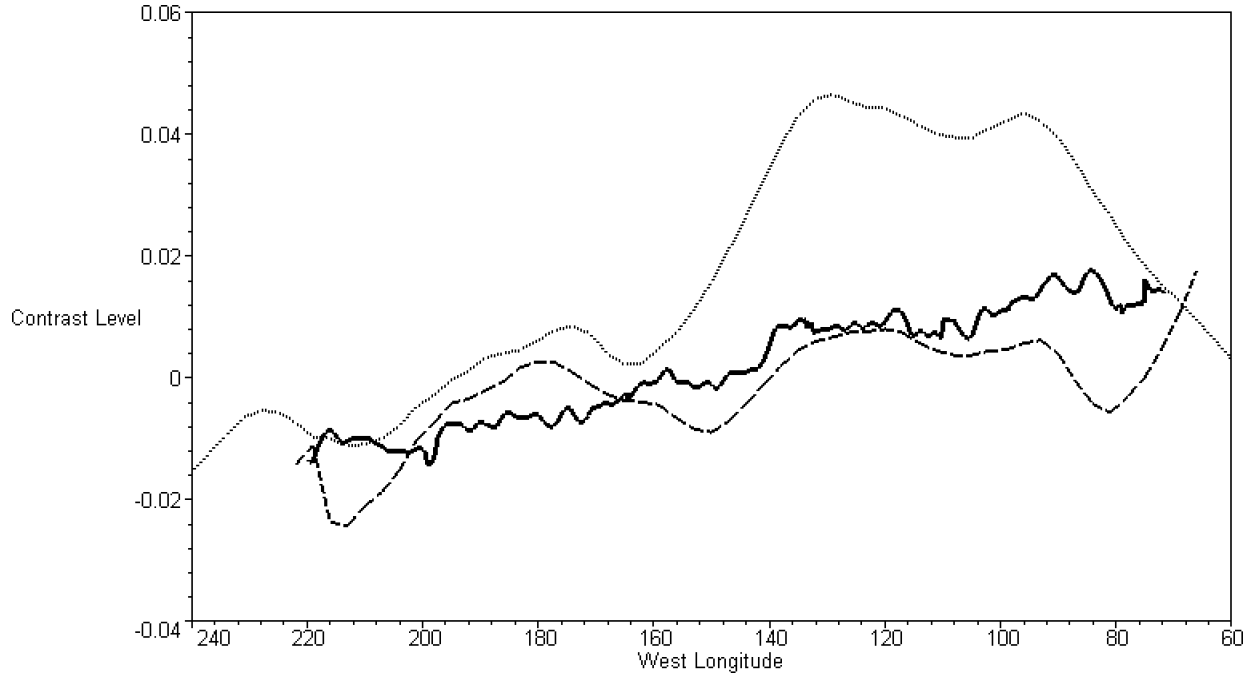

Fig. 6. (Solid line) A equatorial contrast profile (solid line) through the VG1 ORANGE map of Titan shown in Fig. 4, plotting the average of the pixel values within ±6° latitude of the equator, and taken at intervals of 0.5° longitude. The HST F850LP filter profile (dotted line) and HST F673N filter profile (dashed line) plot the average of the pixel values within ±7.5° latitude of the equator, and taken at intervals of 3.0° longitude. These profiles show general agreement in both shape and contrast levels, especially the VG1 ORANGE and HST F673N profiles, which were imaged at similar wavelengths.

Figure 6 shows an equatorial contrast profile (solid line) through the VG1 ORANGE map of Titan shown in Fig. 4, plotting the average of the pixel values within ±6° latitude of the equator (normalized to the average map pixel value), and taken at intervals of 0.5° longitude. This is compared to an HST F850LP filter profile (dotted line) and an HST F673N filter profile (dashed line), plotting the normalized average of the pixel values within ±7.5° latitude of the equator, and taken at intervals of 3.0° longitude. The HST F850LP map profile (dotted line) displays the largest contrast range, ∼ 6%, while the HST F673N (dashed line) and VG1 ORANGE map profiles display an expectedly lower contrast range, ∼ 3%, due to their shorter wavelengths of 673 and ∼ 600 nm, respectively (see Fig. 1). Across the entire VG1 ORANGE map (top pane, Fig. 4), the minimum contrast value is −0.020, the maximum value is +0.031, for a total contrast range of 5.1%.

These profiles show a rough general agreement, in that they all show a rising brightness trend as one moves from west to east, but are limited by the HST resolution of ±6°

(Smith et al., 1996) and the VG1 signal-to-noise ratio. They all begin at a low (negative) contrast level in the dark regions to the west of the 'spit' region, undergo a slight rise as the southern portion of the 'spit' is crossed, display a small dip in contrast level as the darker 'sickle' lane is crossed, and finally rise to a maximum positive contrast level and drop back off again as the Titan bright region is crossed. Note that the VG1 ORANGE profile does not display the saddle behavior when crossing the Titan bright region that is present in both the HST F850LP and HST F673N profiles. This is perhaps due to the fact that the brightness of the western end of the Titan bright region in the VG1 ORANGE map (top pane, Fig. 4) has been somewhat diminished due to its relatively low brightness level in the middle series of VG1 ORANGE images (center pane, Fig. 3). When all nine final images are averaged together to form the final map, the western end of the bright region suffers a diminution in its brightness level which the eastern end does not suffer—leading to the profile shown in Fig. 6.

3.3. Rotation period determination

The time span of nearly 14 years between the Voyager 1 Titan flyby in November of 1980 and the HST observations of Titan acquired in October of 1994 (Smith et al., 1996) provide a unique opportunity to check the rotation period of Titan based upon surface feature images, in addition to the light curve (Lemmon et al., 1995) and radar investigations (Muhleman et al., 1995) that have been performed previously. Visual inspection of the map produced from the VG1 ORANGE images and the map produced from the HST F673N filter observations (both shown in Fig. 4) indicate that Titan's rotation period is very close to being synchronous with its orbital period (hence the good agreement between the various maps in Fig. 4)—assuming that one can eliminate the possibility of aliasing based upon previous rotation period determinations (Muhleman et al., 1995; Lemmon et al., 1995; Smith et al., 1996), which are all close to the orbital period.

In order to quantify the Titan rotation period, the map produced from the VG1 ORANGE images was reduced in pixel scale, from 0.2° by 0.2° to the same 3° by 3° scale as the HST F673N and HST F850LP maps (Smith et al., 1996), and a cross-correlation performed between the values of the corresponding pixels in the two maps. To check the alignment of the features on the two images, the longitude values of the pixels in the original VG1 ORANGE map were then shifted both east and west in 0.5° increments, the map again degraded in pixel scale, and the cross-correlation re-performed. This procedure produced the graph shown in Fig. 7, which shows that the maximum correlation between the two maps occurs when the VG1 ORANGE map is shifted $2.0° \pm 6.4°$ to the west as compared to the HST F673N map and $3.2° \pm 9.9°$ to the west as compared to the HST F850LP map (FWHM error above $r = 0.50$). This gives an average apparent surface feature longitude offset between the VG1 and HST observations (1980 to 1994) of $2.6° \pm 5.9°$ west (essentially 0° offset, within accuracy limits).

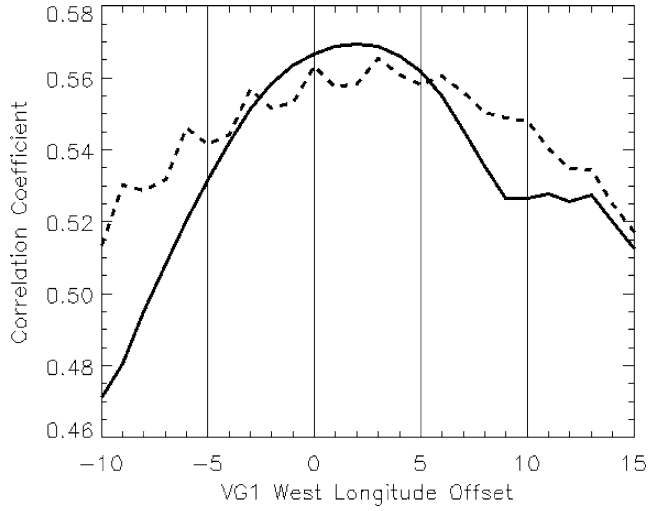

Fig. 7. The cross-correlation of a resolution degraded VG1 ORANGE filter image map with (1) the HST F673N filter map (solid line), and (2) the HST F850LP filter map (dashed line) of Titan's surface. The cross-correlation was calculated over a range of West longitude offsets for the VG1 ORANGE filter map. The maximum correlation between the two map sets occur when the VG1 ORANGE filter map is shifted by (1) 2.0° W ±6.4° for the HST F673N map, and (2) 3.2° W ±9.9° for the HST F850LP map (FWHM error above $r = 0.50$). This gives an average surface feature longitude offset between the VG1 and HST observations (1980 to 1994) of 2.6° W ±5.9° (essentially 0° offset, within accuracy limits).

This result implies that (within the accuracy of these measurements) that the surface features on Titan have not detectably shifted over the 14 year time span between the two sets of observations. Solving for the Titan rotation period, T_r, gives:

$$T_r = 15.9458 \pm 0.0016 \text{ days},$$

which can be compared to the value produced by Lemmon et al. (1995):

$$T_r = 15.949 \pm 0.006 \text{ days},$$

and the Titan orbital period, T_o, of (Pater and Lissauer, 2001):

$$T_o = 15.945421 \pm 0.000005 \text{ days}.$$

Note the good agreement with the Lemmon et al. (1995) results and the Titan orbital period. These two results (this study and Lemmon et al., 1995) do not agree with the super-synchronous rotation period of 15.911 days (no error bar given) determined by Muhleman et al. (1995) and the supporting evidence for this provided by Sears et al. (1993). Although a slightly subsynchronous rotation period cannot be excluded by this study (this period and that obtained by Lemmon et al. (1995) are both slightly longer than fully synchronous), a synchronous rotation state appears to be the most likely for Titan, and is within 1/2 standard deviation of the calculated period from this study.

3.4. Implications for optical depth

Gibbard et al. (1999) presents a summary of the optical depths predicted by the McKay et al. (1989) spherical haze model and the Rannou et al. (1995) fractal model. Both models have an optical depth of about 2.5 at 1 micron. At 600 nm, the McKay et al. (1989) spherical model predicts a similar optical depth of a little over 2, but the fractal model of Rannou et al. (1995) predicts an optical depth of 12 or so. Even for conservative scattering, where transmitted light falls off more slowly than $e^{-\tau}$, it seems difficult to reconcile such a high optical depth with the transmission of 5% surface contrasts, observed in the VG1 ORANGE images produced by this study.

While the authors agree that there is ample theoretical and observational support for the hypothesis that Titan's haze is made from fractal aggregate particles, the fractal model of Rannou et al. (1995)—which does well at providing the required opacity at blue and UV wavelengths—appears to overestimate the opacity at 600 nm (for a given red optical depth, fractal models predict a higher opacity at blue wavelengths than models with spherical particles). Another fractal model, that produced by Lemmon (1994) gives a one-way optical depth of 3 at 600 nm, offering better agreement with the empirical results presented in this study. A principal difference between the Rannou et al. (1995) and Lemmon (1994) models is that the former has significant opacity (at all wavelengths) in the lower stratosphere, whereas in the Lemmon (1994) model, haze is assumed to be removed by rainout processes and the haze opacity is set to zero below an altitude of 64 km or so. McKay (personal communication, 2002) reports that the Rannou et al. (1995) model (which fits Voyager high phase angle data very well) appears to have too much opacity low in the atmosphere, as neither the depth of the 619 nm methane band, nor the thermal structure of the atmosphere, are reproduced correctly. A mitigating factor in this apparently too-high opacity is that the aerosols may be preferentially forward-scattering, preserving enough directed flux that surface contrasts may be visible even at opacities high enough that isotropic scatterers would obscure the surface.

3.5. Looking at Titan through 'rose-tinted glasses'

It is perhaps of some interest that the wavelengths discussed here are visible to the human eye. Red laser pointers, for example, operate at wavelengths of 635, 650, or 675 nm. It is therefore logical to ask: could a human observer, unaided by electronic detectors, see Titan's surface? Even by isolating only this wavelength range by means of red 'sunglasses,' the surface contrasts are only of the order of 5%. Human vision has a radiometric resolution of only 50–200 gray levels (Sidgewick, 1971), so Titan's surface features would therefore be at the limit of, but perhaps just within, human capabilities.

3.6. Implications for the Cassini mission

The detectability of surface contrasts at ∼ 600 nm in the Voyager images is encouraging for the Cassini mission, especially the Imaging Science Subsystem (ISS) and the Visual and Infrared Mapping Spectrometer (VIMS) on the orbiter. The radiometric performances of VIMS and ISS are far superior to those of the Voyager imaging systems, which will allow the small direct (unscattered) component of light reflected from the surface or tropospheric clouds to be detected at smaller contrasts. VIMS will observe Titan in visual and near-IR wavelengths, but only VIMS is sensitive beyond ∼ 1050 nm and can take advantage of methane windows at ∼ 1.6 and 2.0 microns where the optical depth of Titan's haze is well below 1. ISS has several color bandpasses that could be useful for imaging Titan's surface and lower atmosphere (Fig. 8); note that the ISS 940 nm and two other filters were designed for methane windows and should enable better surface imaging than the HST filters. Furthermore, ISS has IR polarizer filters that will aid in imaging the surface at moderate phase angles, by screening out up to 50% of the haze at phase angles near 90° (West and Smith, 1991).

The most interesting implication of the Voyager results is that ISS may be able to acquire very high-resolution (6–60 m/pixel) images of Titan's surface. During close approaches to Titan at ∼ 1000 km VIMS can achieve a pixel scale of 500 m and ISS could, in principle, achieve a pixel scale of 6 m. However, imaging by ISS in the best available methane window at 940 nm requires long exposure times, typically 10 s or longer, to achieve the high SNR required for good images of the surface. Cassini is a very stable platform when controlled by reaction wheels, and unsmeared images can be acquired over long exposure times when Titan's range exceeds ∼ 10,000 km. At closer ranges, however, the images would become increasingly smeared simply due to the change in range to Titan from the start to the end of exposures, limiting the 940 nm images to no better than ∼ 60 m/pixel. Furthermore, when Cassini passes within ∼ 1200 km of Titan it must be controlled by thrusters rather than reaction wheels because of atmospheric torques, further precluding long-exposure images. ISS needs long exposure times at 940 nm because the sensitivity of silicon CCDs drops off rapidly at wavelengths greater than ∼ 750 nm. However, there is a series of methane windows at shorter wavelengths over which ISS has color bandpasses (Fig. 8). The Voyager 600 nm and HST 673 nm results suggest that ISS might be able to image Titan's surface via several bandpasses from 600–800 nm with much shorter exposure times, limiting smear to acceptable levels. These images should have SNRs ∼ 4 times better than the Voyager orange filter images, which will be a significant improvement given that the Voyager surface imaging is very marginal. Competing with this increase in CCD sensitivity as one moves to shorter wavelengths is the corresponding increase in atmospheric optical depth (discussed in Section 3.4), and it remains an

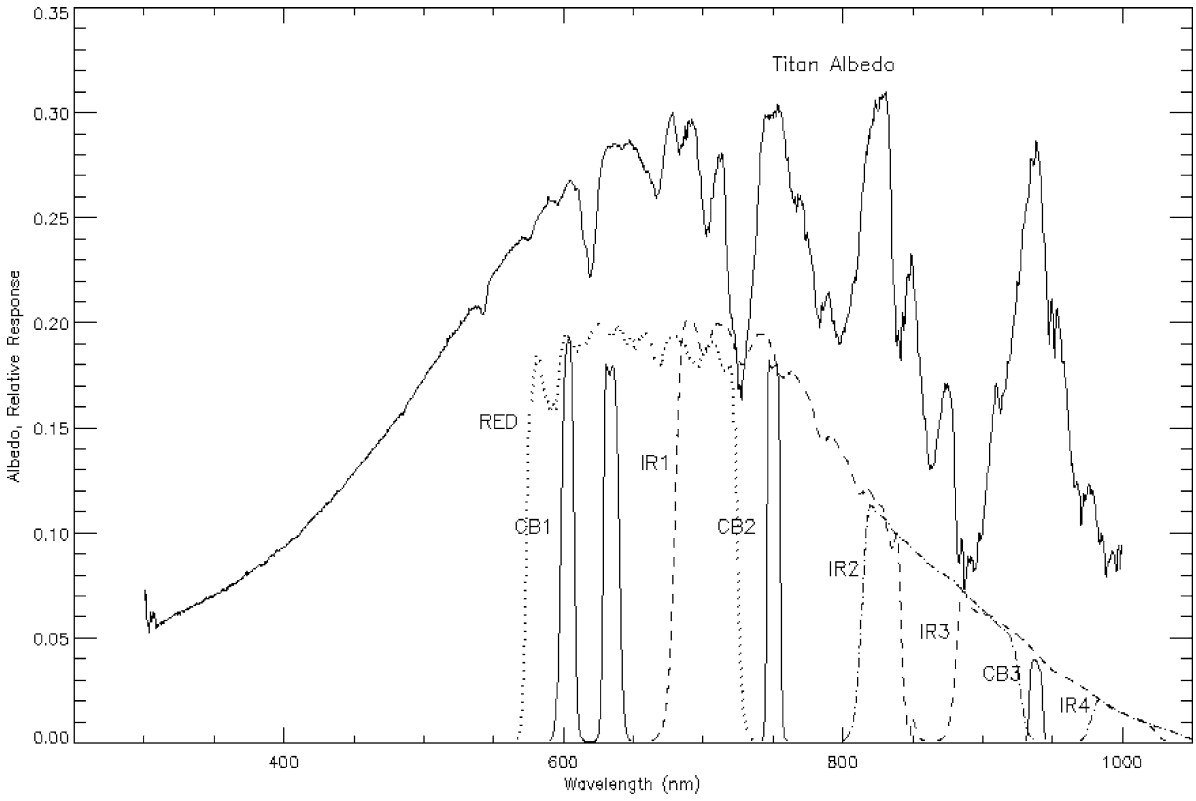

Fig. 8. Relative response of selected Cassini ISS filters compared with a Titan albedo spectrum from Karkoschka (1995) for reference (upper curve). Shown are the response curves for the RED filter (dotted), infrared filters IR1 through IR4 (alternating dashed and dot-dashed), and continuum band filters CB1 through CB3 (solid). Note that these ISS continuum band filters were designed for methane windows and should therefore enable better surface imaging than the HST filters. Furthermore, ISS has IR polarizer filters that will screen out up to 50% of the haze at phase angles near 90° (West and Smith, 1991).

open question as to which of these effects will override the other. If such high-resolution images can be acquired, it may reveal new classes of phenomena and will help place images from the Huygen's probe into a more global context.

Titan's surface albedo patterns appear to vary at different wavelengths (e.g., Fig. 3), which may be due to marginal SNRs or resolution, or imperfect atmospheric corrections, but might also be due to near-IR color variations on Titan's surface. If there are strong color variations, then VIMS and ISS should be able to map color units. Combined with Radar images, Cassini could return a very rich dataset on Titan's surface.

The largest uncertainty facing the ISS and VIMS experiments for imaging Titan's surface is that the albedo patterns seen at scales of $\sim$ 100 km (comparable to the atmospheric scale height) could be carried diffusely through the atmosphere. If this is the case, then it may be impossible to image Titan's surface from outside the atmosphere at better than $\sim$ 100 km scales, except with radar. The Voyager images seem to show features of about 2°–3° in size (90–135 km), which is encouraging but not conclusive, given that the detections are marginal. Cassini ISS or VIMS will need to detect features much smaller than 100 km to clearly demonstrate that a significant percentage of the light reflected from the surface can pass through the atmosphere without further scattering.

4. Conclusions

This work has identified several features on Titan's surface, both bright and dark, in visible-wavelength (590–600 nm) orange filter images from the Voyager 1 1980 flyby of Titan. These features are consistent between individual VG1 ORANGE images, and substantially agree with maps made by HST at 673 nm and by HST and ground-based telescopes at longer wavelengths. Correlation of features in the VG1 ORANGE map with those in both the HST F673N map and HST F850LP map yield a near-synchronous rotation period for Titan of 15.9458 ± 0.0016 days, with fully synchronous rotation likely (within $1/2$ standard deviation of the calculated period).

The observed contrasts of $\sim$ 5% seen in the VG1 ORANGE images are not compatible with the large haze optical depth of 12 predicted by the fractal haze model of Rannou et al. (1995). The success of these observations also suggests that surface features on Titan might be detectable by the human eye, given proper filtering. From a more practical standpoint, this work indicates that Cassini will be able to sense Titan's surface at a variety of wavelengths in the visible and near-infrared (i.e., not just in the 940 nm window). Both the Cassini ISS and VIMS instruments should be able to exploit these new 'windows.'

References

Combes, M., Vapillon, L., Gendron, E., Coustenis, A., Lai, O., Witternberg, R., Sirdey, R., 1997. Spatially resolved images of Titan by means of adaptive optics. Icarus 129, 482–497.

Coustenis, A., Lellouch, E., Maillard, J.P., McKay, C.P., 1995. Titan's surface: composition and variability from the near-infrared albedo. Icarus 118, 87–104.

Coustenis, A., Gendron, E., Lai, O., Veran, J.P., Woillez, J., Combes, M., Vapillon, L., Fusco, T., Mugnier, L., Rannou, P., 2001. Images of Titan at 1.3 and 1.6 μm with adaptive optics at the CFHT. Icarus 154, 501–515.

Danielson, G.E., Kupferman, P.N., Johnson, T.V., Soderblom, L.A., 1981. Radiometric performance of the Voyager cameras. J. Geophys. Res. 86, 8683–8689.

Gibbard, S.G., Macintosh, B., Gavel, D., Max, C.E., de Pater, I., Ghez, A.M., Young, E.F., McKay, C.P., 1999. Titan: high resolution speckle images from the Keck telescope. Icarus 139, 189–201.

Griffith, C.A., 1993. Evidence for surface heterogeneity on Titan. Nature 364, 511–514.

Instrument Catalogue NA1, 2000. Description of the Voyager 1, Imaging Science Subsystem, Narrow Angle camera, from the Planetary Data System (PDS) Rings Node: http://ringmaster.arc.nasa.gov.

Instrument Catalogue WA1, 2000. Description of the Voyager 1, Imaging Science Subsystem, Wide Angle camera, from the Planetary Data System (PDS) Rings Node: http://ringmaster.arc.nasa.gov.

Karkoschka, E., 1995. Spectrophotometry of the jovian planets and Titan at 300- to 1000-nm wavelength: the methane spectrum. Icarus 111, 174–192.

Khare, B.N., Sagen, C., Arakawa, E.T., Suits, F., Callcott, T.A., Williams, M.W., 1984. Optical constants of organic tholins produced in a simulated titanian atmosphere: from soft X-ray to microwave frequencies. Icarus 60, 127–137.

Lemmon, M.T., 1993. Titan's rotation: surface feature observed. Icarus 103, 329–332.

Lemmon, M.T., 1994. Properties of Titan's haze and surface. PhD thesis. University of Arizona.

Lemmon, M.T., Karkoschka, T.E., Tomasko, M., 1995. Titan's rotational lightcurve. Icarus 113, 27–38.

Lorenz, R.D., Lunine, J.I., 1997. Titan's surface reviewed: the nature of bright and dark terrain. Planet. Space Sci. 45 (8), 981–992.

McEwen, A.S., 1991. Photometric functions for photoclinomery and other applications. Icarus 92, 298–311.

McKay, C.P., Pollack, J.B., Courtin, R., 1989. The thermal structure of Titan's atmosphere. Icarus 80, 23–53.

Meier, R., Smith, B.A., Owen, T.C., Terrile, R.J., 2000. The surface of Titan from NICMOS observations with the Hubble Space Telescope. Icarus 145, 462–473.

Muhleman, D.O., Grossman, A.W., Butler, B.J., 1995. Radar investigations of Mars, Mercury, and Titan. Annu. Rev. Earth Planet. Sci. 23, 337–374.

Noll, K.S., Knacke, R.F., 1993. Titan: 1–5 μm photometry and spectrophotometry and a search for variability. Icarus 101, 272–281.

Pater, I., Lissauer, J.J., 2001. Planetary Sciences. Cambridge Univ. Press, Cambridge, MA.

Rannou, P., Cabane, M., Chassefiere, E., Botet, R., McKay, C.P., Courtin, R., 1995. Titan's geometric albedo: role of the fractal structure of the aerosols. Icarus 118, 355–372.

Sears, W.D., Lunine, J.I., Greenberg, R., 1993. Equilibrium nonsynchronous rotation of Titan. Icarus 105, 259–262.

Sidgewick, J.B., 1971. Amateur Astronomers Handbook. Dover, New York.

Smith, B.A., 26 colleagues, 1981. Encounter with Saturn: Voyager 1 imaging science results. Science 212, 163–191.

Smith, B.A., 28 colleagues, 1982. A new look at the Saturn system: the Voyager 2 images. Science 215, 504–537.

Smith, P.H., Lemmon, M.T., Lorenz, R.D., 1996. Titan's surface revealed by HST imaging. Icarus 119, 336–349.

Stammes, P., 1992. The detectability of Titan's surface in the near-infrared. In: Symposium on Titan. In: ESA SP, vol. 338, pp. 205–210.

Tomasko, M.S., Pope, S., Kerola, D., Smith, P., Giver, L., 1989. Constraints on haze and cloud structure from Titan's albedo between 1 and 2.5 μm. Bull. Am. Astron. Soc. 21, 961. Abstract.

West, R.A., Smith, P.H., 1991. Evidence for aggregate particles in the atmospheres of Titan and Jupiter. Icarus 90, 330–333.